Modeling Electroporation in a Single Cell

Wanda Krassowska and Petar D. Filev
Department of Biomedical Engineering, Duke University, Durham, North Carolina

ABSTRACT Electroporation uses electric pulses to promote delivery of DNA and drugs into cells. This study presents a model of electroporation in a spherical cell exposed to an electric field. The model determines transmembrane potential, number of pores, and distribution of pore radii as functions of time and position on the cell surface. For a 1-ms, 40 kV/m pulse, electroporation consists of three stages: charging of the cell membrane (0–0.51 μs), creation of pores (0.51–1.43 μs), and evolution of pore radii (1.43 μs to 1 ms). This pulse creates ~341,000 pores, of which 97.8% are small ($\approx$1 nm radius) and 2.2% are large. The average radius of large pores is 22.8 $\pm$ 18.7 nm, although some pores grow to 419 nm. The highest pore density occurs on the depolarized and hyperpolarized poles but the largest pores are on the border of the electroporated regions of the cell. Despite their much smaller number, large pores comprise 95.3% of the total pore area and contribute 66% to the increased cell conductance. For stronger pulses, pore area and cell conductance increase, but these increases are due to the creation of small pores; the number and size of large pores do not increase.

INTRODUCTION

Electroporation is a technique that uses electric pulses to create transient pores in the cell membrane, which promote the delivery of biologically active molecules into cells (1–4). Despite great interest in this technique, its practical applications are hampered by the lack of a good understanding of the processes taking place during electroporation. Of particular interest is the electroporation process occurring in an isolated cell, since the vast majority of practical applications involve either cell suspensions, tissues composed of cells that are not connected by gap junctions, or, more recently, single cells in microfluidic devices. Hence, numerous studies use a variety of experimental techniques, such as uptake of fluorescent molecules (5,6), imaging of the cell's transmembrane potential (7), or measuring cell's impedance (8) to provide insight into cell electroporation. Nevertheless, some questions cannot be answered with available experimental techniques. Thus, there is a need for supplementing experimental knowledge with a theoretical model.

Currently, the models of electroporation fall into two groups. The models from the first group focus on reproducing the *temporal* process of creation and evolution of pores, but the spatial distributions of the electric potential, pore density, and other quantities are either ignored or represented in a very simplified manner. Most of these models focus on a uniformly polarized membrane patch, often represented by an electrical circuit analog (9–13). In some studies, a pair of such circuits is connected to represent the depolarized and hyperpolarized regions of the cell membrane (14,15). It is unclear to what extent the results from these models reflect electroporation in an actual cell.

The models from the second group take the opposite approach. They solve detailed boundary value problems to determine the *spatial* distribution of the electric potential, the field, and in some cases, the transmembrane potential as well. However, the temporal aspects of electroporation are in these studies either very simplified or altogether absent. In studying single cells, models in this group compute the transmembrane potential (V_m) assuming intact membrane, and use the magnitude of V_m to assess the extent of electroporation (16–19). Some researchers imitate electroporation by increasing membrane conductance in the electroporated regions. This approach allows them to reproduce the experimentally measured distribution of V_m (7,20), tissue impedance (21), and uptake of small molecules (22), and to study electroporation in multicellular systems with irregular shapes (23). Such an increase in membrane conductance indeed accompanies electroporation, but in these studies, the increase was fitted to the data rather than computed from a model.

A few recent studies attempt to combine the two approaches by incorporating the dynamics of electroporation into detailed models of a single cell. A previous model from our group (24), as well as recent work of Weaver's group (25,26), includes explicit creation of pores in the cell membrane. However, these models assume that all pores have the same size, which does not change with time. Thus, these models do not reflect the growth or shrinkage of pores and the resulting distribution of pore sizes. Both creation and growth of pores are included in a spherical cell model of Joshi et al. (27–29). The first version of their model (27) assumes incorrectly that the spatial distribution of V_m is always cosinusoidal, which prevents it from reproducing the flattening of V_m in electroporated regions. This flattening is a defining feature of electroporation in spatially extended systems: it has been observed in experiments (7) and it greatly affects the growth of pores. The assumption of cosinusoidal

Submitted July 28, 2006, and accepted for publication September 28, 2006.

Address reprint requests to W. Krassowska, E-mail: wanda.krassowska@duke.edu.

0006-3495/07/01/404/14 $2.00

doi: 10.1529/biophysj.106.094235

V_m has been dropped in their later model (28), but to date, their studies involved only very short pulses, up to a microsecond in duration. Moreover, it appears that Joshi et al. never used their models to examine *spatial* distributions of V_m, pore density, or pore radii.

The study presented here builds on these earlier attempts and develops a model of cell electroporation in which temporal and spatial aspects are given equal importance, and which can study electroporation on a timescale of milliseconds. Methods describes the main features of the model that allow it to compute transmembrane potential, number of pores, and the distribution of pore radii as functions of both time and position on the cell surface. To do so without prohibitive computational costs, our model relies on asymptotic approximations of the fundamental equations governing creation and evolution of pores, which are developed in our previous work (12,30,31). Results presents a detailed analysis of creation and evolution of pores in a spherical cell of 50-μm radius, exposed to a 40-kV/m electric field for 1 ms. This section also shows how the number and size of pores, as well as their distribution on the cell surface, depend on the strength of the electric pulse, and compares cell electroporation with that of a membrane patch. Finally, Discussion evaluates the predictions of the model in view of available experimental evidence and illustrates how the insight from the model can aid the interpretation of experiments.

MODEL

Mathematical description of electroporation in a single cell

Electric potentials

This study considers a spherical cell of radius a immersed in a conductive medium and exposed to an electric field of strength E. The intracellular and extracellular potentials, Φ_i and Φ_e, are governed by Laplace's equations,

$$\nabla^2\Phi_i = 0\,(\text{inside cell}) \quad \text{and} \quad \nabla^2\Phi_e = 0\,(\text{outside cell}). \tag{1}$$

The external field E is included as a condition on Φ_e,

$$\Phi_e(t,\rho,\theta) = -E\rho\cos\theta \text{ as } \rho \to \infty, \tag{2}$$

where ρ is the distance from the center of the cell and θ is the polar angle measured with respect to the direction of the field E. The current density is continuous across the cell membrane,

$$\begin{aligned} -\hat{n}\cdot(s_i\nabla\Phi_i) &= -\hat{n}\cdot(s_e\nabla\Phi_e) \\ &= C_m\frac{\partial V_m}{\partial t} + g_l(V_m - V_{rest}) + I_p, \end{aligned} \tag{3}$$

where $\hat{n}$ is the outward unit vector normal to the membrane surface, $V_m(t,\theta) \equiv \Phi_i(t,a,\theta) - \Phi_e(t,a,\theta)$ is the transmembrane potential, and all parameters are defined in Table 1. The right-hand side of Eq. 3 shows that the transmembrane current density consists of the capacitive current, current through protein channels, and current through electropores $I_p(t,\theta)$. This formulation includes two simplifications. First, the membrane capacitance C_m is assumed constant, even though it is expected to decrease as a result of pore creation and growth. However, the change in C_m measured experimentally was found to be $<2\%$ (32), which justifies this simplification. Second, the current through protein channels is approximated by a constant leakage conductance g_l. The model can be easily extended by incorporating equations describing the dynamics of this current (33–36). However, our previous study (34) has found that the current through active channels has only a second-order effect on the process of electroporation.

In the context of a boundary value problem, the current through electropores, $I_p(t,\theta)$, is a continuous function of a polar angle θ. In actual simulations, cell surface is discretized in θ from 0 to π with the step of $\Delta\theta$, so that each discrete angle θ represents a portion ΔA of the cell area. If ΔA associated with a discrete angle θ contains K^θ pores, then the total current through these pores is computed by adding

TABLE 1 Parameters of the cell electroporation model

Symbol	Value	Definition and source
a	50 μm	Cell radius (44).
C_m	10^{-2} F m^{-2}	Surface capacitance of the membrane (44).
g_l	2 S m^{-2}	Surface conductance of the membrane (44).
s_i	0.455 S m^{-1}	Intracellular conductivity (44).
s_e	5 S m^{-1}	Extracellular conductivity (44).
s	2 S m^{-1}	Conductivity of the solution filling the pore (13).
V_{rest}	-0.08 V	Rest potential (62).
h	5×10^{-9} m	Membrane thickness (39).
α	1×10^{9} m^{-2} s^{-1}	Creation rate coefficient (24).
V_{ep}	0.258 V	Characteristic voltage of electroporation (24).
N_0	1.5×10^{9} m^{-2}	Equilibrium pore density at $V_m = 0$ (24).
r_*	0.51×10^{-9} m	Minimum radius of hydrophilic pores (39).
r_m	0.8×10^{-9} m	Minimum energy radius at $V_m = 0$ (39).
q	$\equiv (r_m/r_*)^2$	Constant in Eq. 7 for pore creation rate (24).
D	5×10^{-14} m^2 s^{-1}	Diffusion coefficient for pore radius (11).
β	1.4×10^{-19} J	Steric repulsion energy (12).
γ	1.8×10^{-11} J m^{-1}	Edge energy (11,39).
σ_0	1×10^{-6} J m^{-2}	Tension of the bilayer without pores (63).
σ'	2×10^{-2} J m^{-2}	Tension of hydrocarbon-water interface (64).
F_{max}	0.70×10^{-9} N V^{-2}	Max electric force for $V_m = 1$ V (31).
r_h	0.97×10^{-9} m	Constant in Eq. 10 for advection velocity (31).
r_t	0.31×10^{-9} m	Constant in Eq. 10 for advection velocity (31).
T	310 K	Absolute temperature (37°C).

currents through all of them. Thus, the corresponding current density is

$$I_{\mathrm{p}}(t,\theta)=\sum_{\mathrm{j}=1}^{\mathrm{K}^{\theta}} i_{\mathrm{p}}(r_{\mathrm{j}}^{\theta},V_{\mathrm{m}})/\Delta A, \tag{4}$$

where i_{p} is the current-voltage relationship of an individual pore,

$$i_{\mathrm{p}}(r,V_{\mathrm{m}})=\frac{V_{\mathrm{m}}}{R_{\mathrm{p}}+R_{\mathrm{i}}}. \tag{5}$$

Large pores cannot maintain the same voltage drop V_{m} that develops across intact membrane. To account for the decrease of the transpore voltage, Eq. 5 assumes that V_{m} occurs across the pore resistance, $R_{\mathrm{p}}=h/(\pi s r^2)$, and the input resistance, $R_{\mathrm{i}}=1/(2sr)$, connected in series (37,38), where h is the membrane thickness and s is the conductivity of the solution filling the pore. Thus, Eq. 5 gives a nonlinear relationship between the pore area and its conductance. However, Eq. 5 does not account for the interaction of ions with the pore walls, which has been represented by an energy barrier (39,40) or steric hindrance of ions (38).

For $t<0$, field $E=0$ and the potentials have values

$$\begin{aligned}&\Phi_{\mathrm{i}}(0,\rho,\theta)=V_{\mathrm{rest}}\,(\text{inside cell}) \quad \text{and}\\ &\Phi_{\mathrm{e}}(0,\rho,\theta)=0\,(\text{outside cell}),\end{aligned} \tag{6}$$

i.e., the cell is initially at its rest potential V_{rest}. For $t\geq 0$, E is set to a nonzero constant and the potentials evolve in time according to Eqs. 1–3, starting from the initial condition given in Eq. 6.

Nucleation of pores

This study concentrates on the hydrophilic pores that are ion-permeable and thus able to conduct current. The model assumes that such pores appear with an initial radius r_* at a rate determined by an ordinary differential equation,

$$\frac{dN}{dt}=\alpha e^{(V_{\mathrm{m}}/V_{\mathrm{ep}})^2}\left(1-\frac{N}{N_{\mathrm{eq}}(V_{\mathrm{m}})}\right), \tag{7}$$

where $N(t,\theta)$ is the pore density and N_{eq} is the equilibrium pore density for a given voltage V_{m}:

$$N_{\mathrm{eq}}(V_{\mathrm{m}})=N_0 e^{q(V_{\mathrm{m}}/V_{\mathrm{ep}})^2}. \tag{8}$$

All constants are defined in Table 1. Equation 7 is solved with the initial condition $N(0,\theta)=0$ (no pores). Further details of the model of pore creation can be found in our previous publications (12,24).

Note that Eq. 7 describes not only creation of pores but also their resealing: after the pulse has created a certain number of pores, the pore density N becomes larger than N_0, the equilibrium pore density for $V_{\mathrm{m}}=0$. Hence, if the pulse is turned off and V_{m} drops to zero, the right-hand side of Eq. 7 becomes negative and the pore density N starts decreasing.

Evolution of pore radii

The pores that are initially created with radius r_* change size to minimize the energy of the entire lipid bilayer. For a cell with a total number of K pores, the rate of change of their radii, r_{j}, is determined by a set of ordinary differential equations,

$$\frac{dr_{\mathrm{j}}}{dt}=U(r_{\mathrm{j}},V_{\mathrm{m}},\sigma_{\mathrm{eff}}),\quad j=1,2,\ldots,K, \tag{9}$$

where U is the advection velocity given by

$$\begin{aligned}U(r,V_{\mathrm{m}},\sigma_{\mathrm{eff}})=&\frac{D}{kT}\left\{\frac{V_{\mathrm{m}}^2F_{\max}}{1+r_{\mathrm{h}}/(r+r_{\mathrm{t}})}+4\beta\left(\frac{r_*}{r}\right)^4\frac{1}{r}\right.\\ &\left.-2\pi\gamma+2\pi\sigma_{\mathrm{eff}}r\right\}\text{ in } r\geq r_*.\end{aligned} \tag{10}$$

Here, the first term accounts for the electric force induced by the local transmembrane potential $V_{\mathrm{m}}(t,\theta)$; the second, for the steric repulsion of lipid heads; the third, for the line tension acting on the pore perimeter; and the fourth, for the surface tension of the cell membrane. All parameters are defined in Table 1. The first term in Eq. 10, for the electric force, applies to pores of arbitrary size with toroidal inner surface (31). The last term contains the effective tension of the membrane, σ_{eff}, which is a function of A_{p}, the combined area of all pores existing on the cell (30),

$$\sigma_{\mathrm{eff}}(A_{\mathrm{p}})=2\sigma'-\frac{2\sigma'-\sigma_0}{(1-A_{\mathrm{p}}/A)^2}, \tag{11}$$

where σ_0 is the tension of the membrane without pores, σ' is the energy per area of the hydrocarbon-water interface, $A_{\mathrm{p}}=\sum_{\mathrm{j}=1}^{\mathrm{K}}\pi r_{\mathrm{j}}^2$, and A is the surface area of the cell. This study assumes that changes of cell area, volume, and shape can be ignored for millisecond pulses considered here.

Numerical implementation

The numerical solution of the governing Eqs. 1–3, 6, 7, and 9 is based on our previous studies (13,24). Briefly, the spherical cell of radius a is immersed in a spherical shell of extracellular fluid of thickness $2a$. Both intra- and extracellular space are discretized using spherical coordinates; discretization steps are $\Delta\theta=\pi/128$ and $\Delta\rho=3a/60$. Equation 1 governing potentials Φ_{i} and Φ_{e} are transformed using the finite difference method into a set of linear equations. The external electric field is imposed as a Dirichlet boundary condition on the potential Φ_{e} along the outer boundary of the extracellular shell ($\rho=3a$) consistent with Eq. 2. Continuity of current across the membrane, given by Eq. 3, is imposed treating the values of current through electropores, I_{p}^{θ}, as known. (For a discretized cell, superscripts are used to distinguish membrane-related quantities that change with the polar angle from quantities that apply to the whole cell, which have no superscripts; see next subsection.) The resulting set of equations is solved at each time step, yielding

potentials Φ_i and Φ_e. The transmembrane potential V_m^θ is computed by subtracting the value of Φ_e, taken at a node adjacent to the membrane, from the value of Φ_i on the opposite side of the membrane.

Next, for each discrete angle θ on the membrane, new values of the number of pores and their radii are computed. To speed up computations, the model keeps track of two distinct populations of pores. *Small pores*, whose radii congregate near the minimum-energy radius of ~1 nm, are accounted for by the local pore density N^θ. All pores in this population are assumed to have the same radius r_{min}^θ, which evolves according to Eq. 9 with r_j replaced by r_{min}^θ. *Large pores*, whose radii are larger than r_{min}^θ, are represented individually: the radius of each pore evolves according to Eq. 9. The exchange of pores between these two populations proceeds as follows. Pores created according to Eq. 7 are all initially treated as large. Pores remain in the large pore population throughout the initial stage of creation and rapid expansion of pores. Afterward, pore growth slows down and eventually some pores start to shrink. If any large pore shrinks to within 1 pm of r_{min}^θ, it is absorbed into the small pore population, thereby increasing N^θ and decreasing the local number of large pores, K_{lg}^θ. To make sure that the absorption of pores does not introduce artifacts, key simulations were repeated without pore absorption.

Equations 7 and 9 are solved using the midpoint implicit method. The updated vectors V_m^θ, N^θ, K_{lg}^θ, r_{min}^θ and r_j^θ, $j = 1, \ldots K_{lg}^\theta$ are used to compute the current through pores I_p^θ and the effective membrane tension σ_{eff}. The vector I_p^θ will be used in the next time step to determine Φ_i and Φ_e.

Three features of implementation aim at increasing computational efficiency. First, to limit the number of pore radii that need to be updated by solving Eqs. 9, pores created at the same time-step are treated as a group rather than individually. Second, having two distinct populations of small and large pores further limits the number of independently-evolving pore radii. For example, a 40 kV/m field creates 341,000 pores. All pores belong to the large pore population for only ~2.5 μs; by 100 μs, all but 16,000 pores have been absorbed into the small pore population. Finally, the solution uses adaptive time-stepping. Initially, $\Delta t = 1.5$ ns is used to resolve very fast transients associated with the creation of pores. Once pore creation ends and the dependent variables change less rapidly, Δt is gradually increased to 0.1 μs. The above initial and final Δt yield mean errors in voltage and maximum pore radius <0.1%, and in pore density, below 4%. The simulation of a 1-ms, 40 kV/m pulse takes ~5 min (model implemented in C and running on a 3.4 GHz Pentium 4 processor under CentOS 4.0).

Pore statistics

At a position specified by a polar angle θ, the electroporation process is characterized by the local quantities in Table 2. All these quantities have superscripts indicating their dependence on the polar angle. Five locations on the cell membrane are of particular interest (Fig. 1): the depolarized pole (D), hyperpolarized pole (H), equator (E), and borders between electroporated and nonelectroporating regions (D_b and H_b). Thus, the general superscript θ may be replaced by D, H, etc., indicating the specific location.

TABLE 2 Local characteristics of electroporation

V_m^θ	Transmembrane potential.
K^θ (K_{sm}^θ, K_{lg}^θ)	Number of all (small, large) pores within ΔA surface area associated with one node.
N^θ	Density of small pores ($K_{sm}^\theta = N^\theta \Delta A$).
G^θ (G_{sm}^θ, G_{lg}^θ)	Surface conductance of the membrane (in S/m^2) due to all (small, large) pores.
F^θ (F_{sm}^θ, F_{lg}^θ)	Fractional pore area due to all (small, large) pores, e.g., $F^\theta = \sum_{j=1}^{K^\theta} \pi r_j^2 / \Delta A$.
r_{max}^θ	Maximum local radius.
$\bar{r}^\theta$	Average radius of large pores.

TABLE 3 Characteristics of electroporation in the entire cell

K (K_{sm}, K_{lg})	Number of all (small, large) pores.
G (G_{sm}, G_{lg})	Conductance of the cell (in S) due to all (small, large) pores, e.g., $G = \sum_{j=1}^{128} G^\theta \Delta A$.
F (F_{sm}, F_{lg})	Fractional pore area due to all (small, large) pores, e.g., $F = \sum_{j=1}^{K} \pi r_j^2 / A$.
r_{max}	Maximum radius anywhere on the cell.
$\bar{r}$	Average radius of large pores.
θ_d (θ_h)	Polar angle of the border between electroporated and intact membrane on the depolarized (hyperpolarized) hemisphere.

In the entire cell, the electroporation process is characterized by the quantities in Table 3. These quantities do not

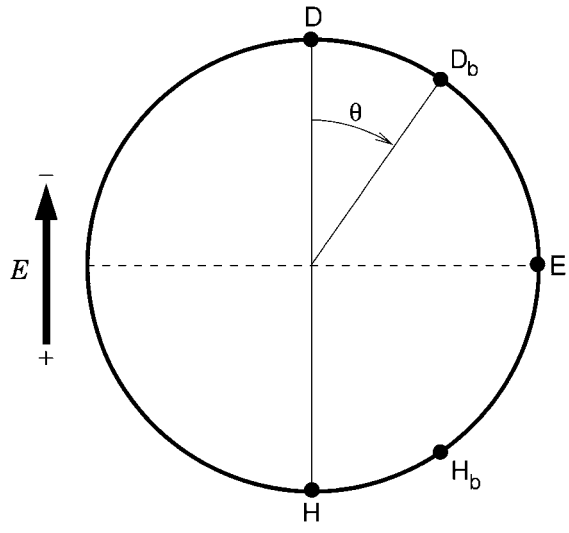

FIGURE 1 Schematic of a spherical cell considered in this study. Locations of particular interest are indicated by labels: D (H), depolarized (hyperpolarized) pole, D_b (H_b), border between electroporated and nonelectroporated region in the depolarized (hyperpolarized) part of the cell, E, cell equator. An arrow indicates the direction of the electric field E, polar angle θ measures the position along the cell circumference.

have any superscripts, which indicates that they apply to the entire cell.

RESULTS

Creation and time evolution of pores

Consider a 50-μm cell exposed to a 40 kV/m electric field for 1 ms. As seen in Fig. 2, the electroporation process can be divided into three distinct stages: charging, pore nucleation, and pore evolution (*dotted vertical lines* separate the stages).

The charging stage starts with the application of the electric field and ends with the formation of the first pore anywhere on the cell membrane. Since the membrane does not yet contain any pores, current I_p in Eq. 3 is zero and the membrane charges like a parallel resistance and capacitance. This passive charging can be seen during the first 0.51 μs in Fig. 2 *A*, when transmembrane potential increases in magnitude from its initial value of $V_{rest} = -0.08$ V according to the formula

$$V_m^\theta = 1.5Ea\cos\theta(1 - e^{-t/\tau}) + V_{rest},$$
$$\text{where} \quad \tau = a\,C_m\left(\frac{1}{s_i} + \frac{1}{2s_e}\right). \tag{12}$$

The charging phase ends at 0.51 μs, when the first pore is created. As expected, this pore appears on the hyperpolarized pole (H) of the cell: during charging, V_m^H has larger magnitude than V_m^D because of the negative V_{rest}.

Pore nucleation at a specific angle θ starts when its transmembrane potential exceeds a threshold value of $\sim$1 V. There is no sharp threshold for electroporation: as expected from Eq. 7, any $V_m > 0$ will create pores but weak pulses may require a very long time (41). Experiments typically use pulses up to milliseconds in duration, and electroporation is identified either by the uptake of small molecules (5,6) or by the decrease in V_m during the pulse (42–44). Using the latter criterion and assuming that a 5% decrease is experimentally detectable, the model's parameter V_{ep} was chosen so that $V_m < 1$ V will be considered subthreshold.

Locations where V_m^θ exceeds threshold experience a dramatic increase in the pore creation rate (Eq. 7), and hence the number of pores increases. These pores add additional pathways for current to cross the membrane, and thus increase its local conductance G^θ. In consequence, V_m^θ no longer follows the charging transient that would be observed in a cell with a passive membrane (Eq. 12). As seen in Fig. 2 *A*, the magnitude of V_m^θ peaks and then decreases.

Since different locations on the cell membrane reach threshold at different times, the timing and the degree of V_m^θ decrease depend on the position. As seen in Fig. 2 *B*, polar regions, D and H, begin the formation of pores the earliest, at 0.65 and 0.51 μs, and they accumulate 8.9×10^3 and 10.1×10^3 pores, respectively (the corresponding pore densities are 3.63×10^{13} and 4.11×10^{13} pores/m^2). Consequently, D and H experience the largest decrease in the magnitude of V_m^θ: by the end of the pulse, V_m^D (V_m^H) discharges from a peak value of 1.34 V (-1.35 V) to 0.38 V (-0.36 V). In contrast, border locations, D_b and H_b, contain only one pore each (pore density of 4.07×10^9 pores/m^2), which were created at 1.5 μs at H_b, and as late as 0.32 ms at D_b. These locations still see a considerable drop in voltage magnitude, from just above $\pm$1 V to 0.65 V (-0.59 V) at D_b (H_b). Interestingly, $V_m^{D_b}$ starts decreasing at 1.5 μs, even though the pore does not form at this location until much later. This example demonstrates that V_m^θ is strongly influenced by the state of the membrane in the adjacent regions and thus it decreases even in the regions of the cell membrane that are not electroporated.

The pore nucleation stage is assumed completed when the relative increase in the total number of pores per time step

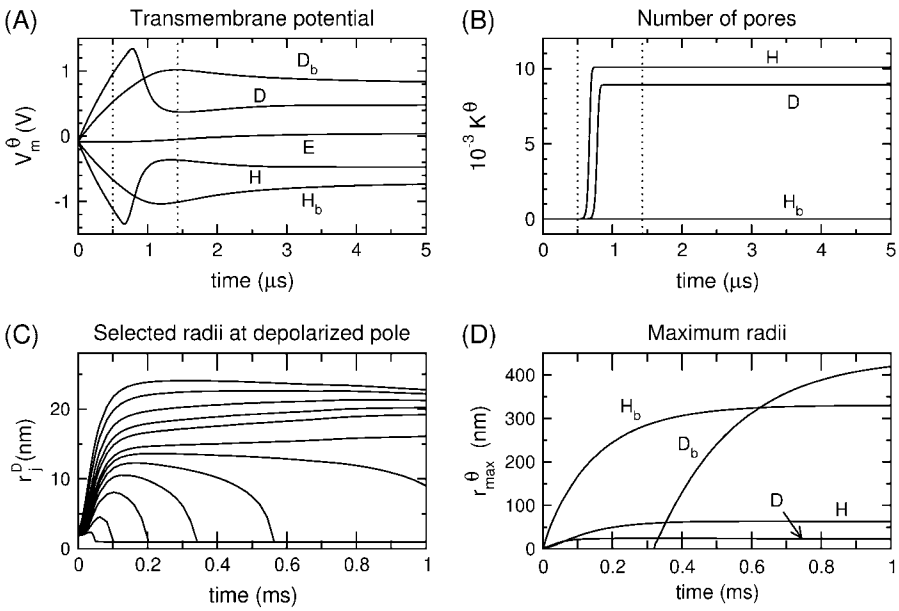

FIGURE 2 Time evolution of electroporation in a cell. (*A*) Transmembrane potential V_m^θ at the locations indicated by labels. (*B*) Number of all pores K^θ at locations D, H, and H_b. There is only one pore at H_b, no pores at D_b or E. K^θ of 10^4 corresponds to a pore density of 4.07×10^{13} pores/m^2. (*C*) Radii r_j^D of 12 selected pores at the depolarized pole. (*D*) Maximum radii r_{max}^θ at locations indicated by labels. The pore at location D_b was created at 0.32 ms. Note the different timescales in panels *A* and *B* versus *C* and *D*. Dotted vertical lines in panels *A* and *B* indicate the start and the end of the pore nucleation stage.

drops below 10^{-6}. According to this definition, in the example of Fig. 2, nucleation ends at 1.43 μs. Even though a few pores may be created after this time (such as at the border regions D_b and H_b), the vast majority of pores are created within the time interval indicated by the dotted vertical lines in Fig. 2.

Pore evolution is a considerably slower process than either pore nucleation or changes in V_m^θ. Pores start growing immediately after they are created but their radii are no more than 5 nm by the end of the nucleation phase. Most of the pore evolution occurs after the creation of new pores has ceased and even after V_m^θ has leveled off, both of which happen within microseconds. In contrast, some pore radii will not reach steady state during the first millisecond of the 40 kV/m pulse (Fig. 2, *C* and *D*) and will continue to evolve, although subsequent changes will be relatively small. Since V_m^θ no longer changes, this adjustment of pore radii is driven by the last two terms of the advection velocity (Eq. 10): the line energy of pore perimeters and the effective tension of the membrane. The latter factor is especially significant: as pores grow, they relieve membrane tension, so the effective membrane tension σ_{eff} decreases (Eq. 11). Because σ_{eff} couples all pores on the cell, pores evolve to minimize not their individual energies but the energy of the entire membrane (30).

The minimization of the membrane energy is the driving factor behind the division of all pores into two populations. As illustrated in Fig. 2 *C* for the depolarized pole, all pores initially grow but soon smaller pores start shrinking and eventually assume a radius of ~1 nm (membrane energy has a local minimum here). These form the population of ''small'' pores. Small pores are subject to resealing (Eq. 7). In experiments, resealing time is highly variable (39,45) but considerably longer than a 1-ms pulse considered here. In the model, the resealing time is on the order of seconds (with parameters of Table 1), so the small pores do not disappear during the pulse.

The remaining pores adjust their radii to a range of 15–25 nm, forming a population of ''large'' pores. Their radii are determined primarily by the local number of pores and local V_m^θ, with some impact from the number of pores on the entire cell. Thus, pore sizes vary with the position on the cell. Fig. 2 *D* shows the radii of the largest pore at locations *D*, *H*, D_b, and H_b (there are no pores at *E*). This figure illustrates the differences in both pore sizes and their rates of change between the polar and border regions of the cell.

Spatial distribution of transmembrane potential and pores

Voltage

Fig. 3 *A* shows how the transmembrane potential V_m changes along the cell circumference. Up to 0.51 μs, V_m maintains a cosinusoidal profile predicted by Eq. 12. By 1.43 μs, large dips develop in the V_m profile at the two polar regions of the cell. These dips are the direct consequence of the creation of pores in these regions. Because at this time all pores are still small and fairly uniform in size (*dashed line* in Fig. 3 *C*), the depth of the dips is related to the number of pores created at any particular location (*heavy line* in Fig. 3 *B*). This relation breaks down as pore radii evolve, and by 1 ms, V_m^θ becomes nearly flat in the electroporated regions of the cell. The magnitude of V_m^θ is larger near the border of the electroporated region, in which fewer pores provide fewer pathways for the transmembrane current.

At 1 ms, transmembrane potential is at its steady state. Note that the nonelectroporated regions of the cell have V_m^θ magnitude considerably lower than they would in absence of

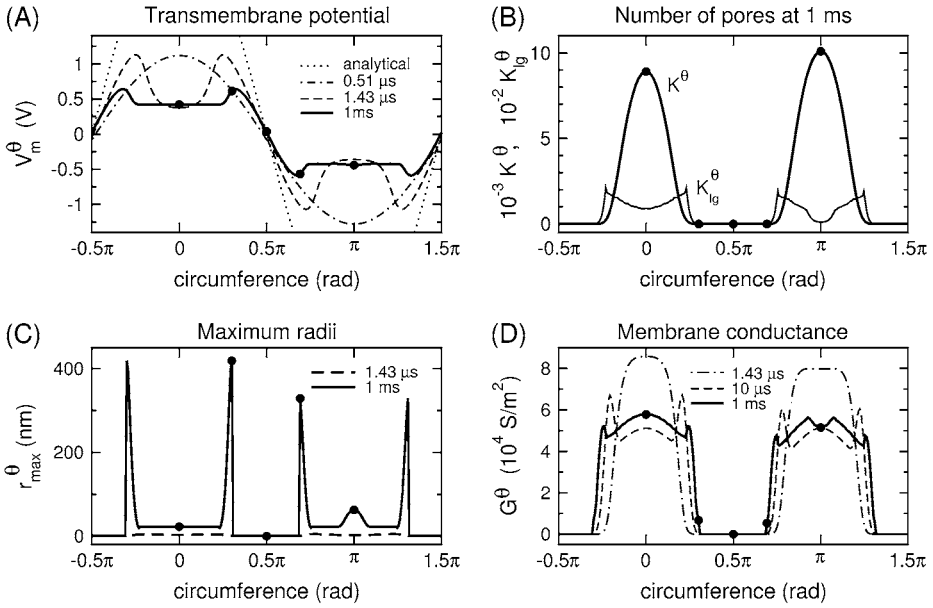

FIGURE 3 Spatial distribution of electroporation in a cell. (*A*) Transmembrane potential V_m^θ at times indicated in the legend. The dotted line is the steady-state potential that would have been achieved without electroporation. The times 0.51 and 1.43 μs are the start and the end of the pore nucleation stage. (*B*) Number of all pores K^θ and number of large pores K_{lg}^θ at 1 ms. Note the 10-fold difference in scales for K^θ and K_{lg}^θ. (*C*) Maximum radius r_{max}^θ at the end of the nucleation stage (1.43 μs) and at 1 ms. (*D*) Membrane conductance G^θ at the times indicated in the legend. In panels *A–D*, solid circles on the 1-ms plots indicate locations *D*, D_b, *E*, H_b, and *H* (*left* to *right*).

electroporation (*dotted line*). It confirms that electroporation lowers the magnitude of V_m^θ not only locally in the regions where the pores are created but also throughout the entire cell.

Pores

Fig. 3 *B* shows the total number of pores K^θ as a function of position on the cell surface. It confirms that the decrease in V_m^θ seen in Fig. 3 *A* is a direct reaction to the creation of pores. There are no pores in the regions around the equator, $0.95 < \theta < 2.17$ rad ($54° < \theta < 124°$), in which V_m^θ has never reached the electroporation threshold.

Of all existing pores, only a small fraction belong to the large pore population, as illustrated by the thin line in Fig. 3 *B* (in interpreting this figure, note that the scale for large pores is 10 times larger than the scale for the small pores). K_{lg}^θ increases as one moves toward the border of the electroporated region: since fewer pores were created there, nearly all of them grow to compensate for their smaller number. As illustrated in Fig. 3 *C*, which shows the maximum pore radii, r_{max}^θ, at each location, some border-zone pores grow to very large sizes and exceed 300 nm. In contrast, the largest pores in the polar regions of the cell, where V_m^θ is flat, have radii of ~23 nm (except near the hyperpolarized pole).

Membrane conductance

The interplay of the pore number and their sizes produces interesting changes in the conductance of the cell membrane (Fig. 3 *D*). The surface conductance G^θ has the largest value early in the electroporating process. For example, at 1.43 μs, when the pores have already been created but are still relatively small, G^D is 8.6×10^4 S/m^2. A visible increase in G^θ is limited to the regions where a significant number of pores are created, i.e., closer to the poles and not in the border zone. As the pore radii evolve in time, the G^θ distribution decreases in magnitude and broadens. By 1 ms, G^D has dropped to 5.8×10^4 S/m^2 and G^{D_b} has increased from zero to 0.68×10^4 S/m^2.

Distribution of pore radii

As seen in Fig. 2 *C*, pores divide themselves into two distinct populations: small pores, with radii close to 1 nm, and large pores, with radii well above 1 nm. Small pores greatly outnumber the large ones (see Fig. 4 for specific numbers). At 1 ms, 97.8% of all pores on a cell are small, and the remaining 2.2% are large. Despite their much greater number, small pores comprise only 4.7% of the total pore area and they contribute 34% to the increased conductance of the cell. In polar regions *D* and *H*, small pores play a larger role: 99% of pores at pole *D* are small, they comprise 19.5% of the local pore area, and account for over half (57.5%) of membrane conductance.

The evolution of radii within the large pore population is illustrated in Fig. 4. At pole *D*, the number of large pores, K_{lg}^D, decreases with time while the distribution of pore radii moves toward larger values, reaching 19.4 ± 3.4 nm (mean and standard deviation) at 1 ms, with 90 large pores. The behavior of large pores depends on their location on the cell. In the polar regions, where V_m^θ is flat, pores behave similarly to the pores at the *D* pole: some shrink and become small, while others continue to grow. Pores from the border zones grow more vigorously to compensate for their much smaller number and reach radii up to 419 nm. However, at 1 ms only

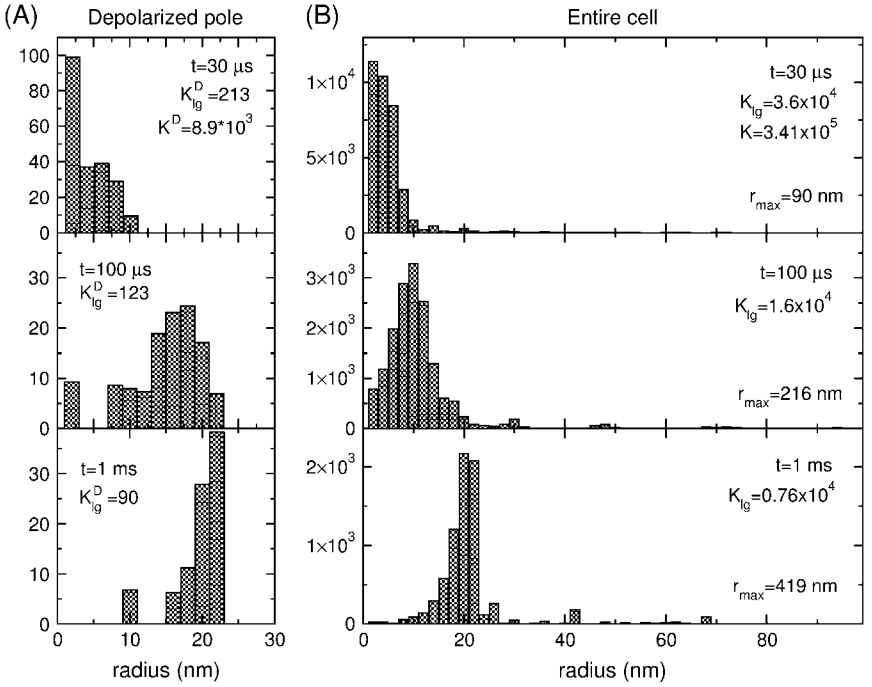

FIGURE 4 Distribution of pore radii at 30 μs, 100 μs, and 1 ms. (*A*) Pores at the depolarized pole *D*. (*B*) Pores on the entire cell. Only large pores are included in the distributions and their number K_{lg} is given on each panel. The total number of pores, *K*, is reported in the upper panels. Two lower panels of panel *B* cover only part of the range of pore radii; maximum radii r_{max} are reported in each panel. The bin width = 2 nm.

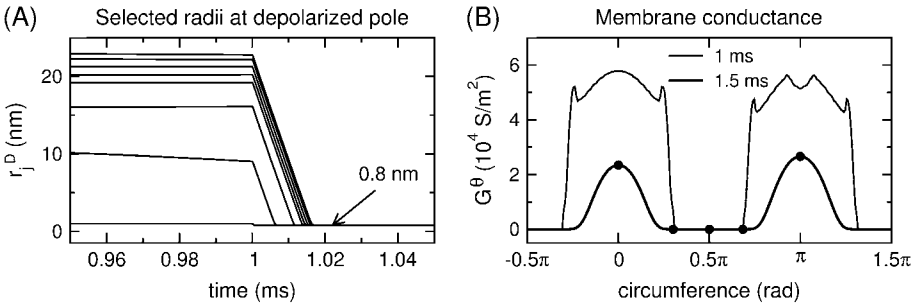

FIGURE 5 Postpulse evolution of the pores in a cell. The electric field has been turned off at 1 ms. (*A*) Radii r_j^D of 12 selected pores (seven large and five small) at the depolarized pole *D*. This panel is a continuation of Fig. 2 *C*. (*B*) Membrane conductance G^θ at the end of the pulse (1 ms, *thin line*) and after the pulse (1.5 ms, *thick line*). Solid circles on the 1.5-ms plots indicate locations *D*, D_b, *E*, H_b, and *H* (*left* to *right*).

91 pores (out of 7600 large pores) have radii above 100 nm. The average radius over all large pores is 22.8 ± 18.7 nm.

Postpulse transient

The electric pulse is terminated at 1 ms. Immediately, the cell membrane starts discharging and 2 μs later, V_m^θ drops to nearly zero. At 0.5 ms after the pulse, the cell is slightly hyperpolarized, with V_m^θ varying from −40 μV at the poles to −105 μV on the equator. In response to the drop in V_m^θ, pores start shrinking rapidly. Fig. 5 *A* shows the postpulse evolution of pore radii at location *D* (it is the continuation of pore evolution shown in Fig. 2 *C*). The large pore population disappears when all large pores have become so small that they are absorbed into the small pore population. This process lasts 15–20 μs, depending on the initial sizes of pores at a given position. This fast shrinkage should not be confused with resealing, which proceeds with a time constant of seconds. Thus, at 0.5 ms after the pulse, all pores are still present but their radii have shrunk to 0.8 nm (local energy minimum for $V_m = 0$).

As a result of pore shrinkage, the fractional pore area decreases over 20-fold, from 0.069% to 0.003% of the cell membrane area. Likewise, membrane conductance decreases: e.g., G^D drops from 5.8×10^4 to 2.4×10^4 S/m^2. Fig. 5 *B* shows the distributions of *G* at the end of a 1-ms pulse and 0.5 ms after its termination. These two distributions differ in both magnitude and shape. In particular, the shape of the postpulse distribution directly reflects the local number of pores (seen in Fig. 3 *B*) since the differences in pore radii no longer exist.

Effects of a nonzero resting potential

The model assumes that a cell is initially at rest, with $V_m^\theta = V_{rest} = -0.08$ V. As a result, the hyperpolarized half of the cell has a head start over the depolarized half as they charge toward the threshold. There are several consequences of this asymmetry.

First, pores in the hyperpolarized half of the cell are created earlier than they are in the depolarized half: the first pore is created at 0.51 μs at location *H* and at 0.65 μs at *D* (Fig. 2 *B*). V_m^θ has a larger peak at *H* (−1.35 V) than at *D* (1.34 V), which leads to 12% more pores (Fig. 2 *B*). This difference in the number of pores results in significant differences in pore evolution (Fig. 2 *D*) and eventually leads to the asymmetry in pore distribution.

At 1 ms, the region next to pole *H* has more pores but fewer of them are large pores: $K_{lg}^H = 11$ and $K_{lg}^D = 90$. The 11 pores at *H* grow to larger radii ($\bar{r}^H = 62.6 \pm 0.2$ nm and $\bar{r}^D = 19.4 \pm 3.4$ nm) but this growth does not quite compensate for their smaller number. Membrane conductance G^θ is smaller on the hyperpolarized half of the cell, except very close to the border zone (Fig. 6 *B*). The transmembrane potential V_m^θ is quite similar in both hemispheres (Fig. 6 *A*). Small differences in V_m^θ reflect the differences in conductance G^θ, with V_m^θ having larger magnitude wherever G^θ is smaller.

Although not apparent in Fig. 6 *A* because of the scale, the cell equator *E* is slightly depolarized. Fig. 7 shows time evolution of V_m^E in more detail. Starting from the rest potential at −0.08 V, V_m^E reaches a peak of 0.039 V at 5.6 μs and then discharges monotonically to 0.021 V at 1 ms. This depolarized value at the equator results from the asymmetry

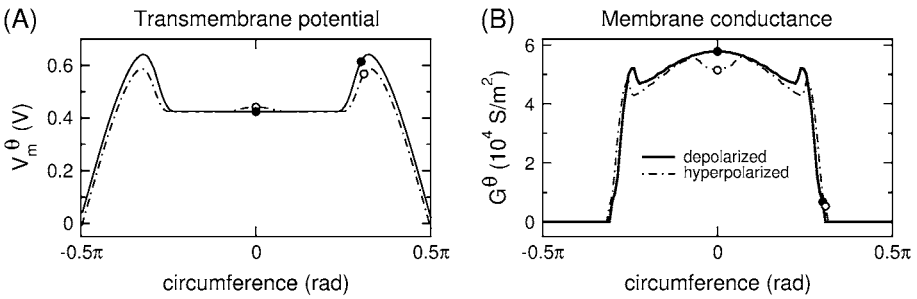

FIGURE 6 Asymmetry of the electroporation process. (*A*) Transmembrane potential over the depolarized and hyperpolarized hemispheres (*overlaid*). (*B*) Membrane conductance, G^θ, over the depolarized and hyperpolarized hemispheres (*overlaid*). In both panels, solid circles indicate the position of the pole *D* and the border D_b; open circles indicate the pole *H* and the border H_b.

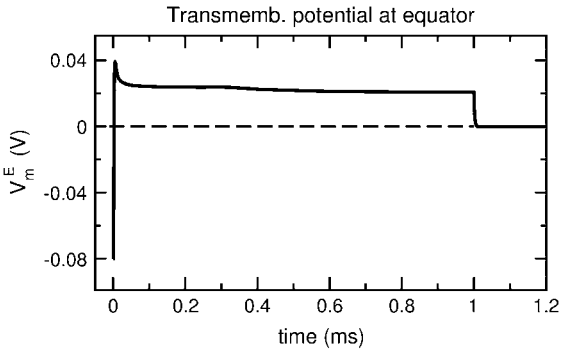

FIGURE 7 Transmembrane potential V_m^E at the equator of the cell. The dashed line indicates $V_m = 0$.

in membrane conductance, specifically from G^{H_b} being higher than G^{D_b}. Postpulse, V_m^E quickly drops to a very small hyperpolarized value of -105 μV.

Effects of pulse strength

The pore distribution depends on the strength of the electric field E applied to the cell, and the model is used to explore this dependence. Fig. 8 illustrates the effect of field strength on the number of pores, their average radius, the area of pores, cell conductance, and the extent of electroporation. The field E ranged from 13 kV/m (close to threshold) to 100 kV/m, and all data were collected at the end of a 1-ms pulse.

As expected, the number of pores increases with the pulse strength but, except for very weak pulses, this increase is due to the creation of small pores. In Fig. 8 *A*, curves representing all pores and small pores overlap and large pores appear to be a negligible fraction of all pores. As seen on the expanded vertical axis in Fig. 8 *B*, the number of large pores K_{lg} initially increases but for E above 40 kV/m, K_{lg} slightly decreases and then levels off at ~7000 pores. Likewise, the average radius of large pores, $\bar{r}$, essentially levels off as the pulse strength increases: for E above 20 kV/m, $\bar{r}$ stays between 20 and 25 nm (Fig. 8 *C*). Despite their limited number and size, large pores continue to contribute significantly to the fractional pore area F (Fig. 8 *D*) and to the increase in cell conductance G (Fig. 8 *E*). For pulses 20 kV/m and below, essentially all increase of F and G is due to large pores. However, as the pulse strength increases, the contribution of small pores increases, especially to G. At $E = 100$ kV/m, 81% of cell conductance is due to small pores.

Fig. 8 *F* shows the extent of electroporation, measured as the polar angle of the border nodes between electroporated and intact regions (θ_d and θ_h). Small fluctuations seen in the curves result from the discretization of the cell's circumference. The figure shows that the extent of electroporation is very similar in both hemispheres. There is some asymmetry that results from the negative rest potential: for $E \geq 20$ kV/m, θ_h is larger; for weaker pulses, θ_d exceeds θ_h. The extent of electroporation grows with the pulse strength but at an increasingly slower rate.

Single cell versus membrane electroporation

In the past, several studies investigated electroporation in a uniformly polarized membrane patch, viewing it as a representation of a depolarized or hyperpolarized polar region of a single cell (13,15,23). Thus, the question arises to what extent electroporation of the membrane resembles electroporation of a single cell. Having previously developed a

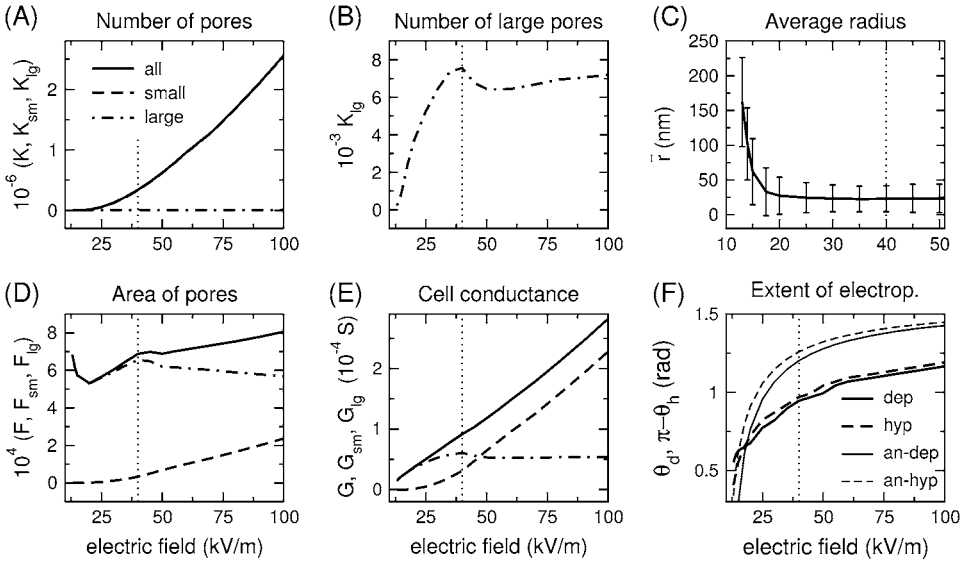

FIGURE 8 Dependence of cell electroporation on field strength. All results were collected at the end of a 1-ms pulse and apply to the whole cell. (*A*) Number of all pores (K) and number of small (K_{sm}) and large (K_{lg}) pores. The lines corresponding to K and K_{sm} overlap. (*B*) Number of pores in large pore population shown on an expanded vertical scale. (*C*) Average radius ($\bar{r}$) of the large pore population. The vertical bars indicate standard deviation. For clarity, the range of the field strengths was truncated to 50 kV/m; $\bar{r}$ continues at the same level beyond 50 kV/m. (*D*) Total area of pores reported as a fraction of the cell surface area. (*E*) Total conductance of the cell membrane. (*F*) Extent of electroporation in the cell measured by the polar radii θ_d and θ_h. To facilitate comparison with θ_d, the figure plots π–θ_h. The lines labeled *an-dep* and *an-hyp* show the extent of electroporation estimated from Eq. 12 for the depolarized and hyperpolarized hemisphere, respectively. The legend in panel *A* applies also to panels *B*, *D*, and *E*. Dotted vertical line indicates the electric field of 40 kV/m, i.e., the default field-strength used throughout this article.

model of electroporating membrane (13), we have the tools to address this question. We have adjusted parameters of our membrane model to correspond to those of the cell and ran simulations for the range of pulse strengths corresponding to those in Fig. 8. The results indicate that electroporation in a membrane patch indeed closely resembles electroporation at the polar regions: the number of pores and their area agree within an order of magnitude. Number of pores grows with the pulse strength but in both cases, this growth is due to small pores. The average radius of large pores decreases with the pulse strength and levels off at 20–25 nm. Above 45 kV/m in the cell (3.75 V in the membrane), large pores disappear altogether and only small pores are being created.

However, neither polar regions nor the membrane patch reflects electroporation in the cell as a whole. In a patch, the number of large pores decreases to zero as pulse strength increases but in the cell, it levels off (Fig. 8 *B*). Finally, in a patch the large pore population becomes increasingly more compact for stronger pulses so that all large pores have essentially the same radius (13). This accumulation of pore radii also occurs at any single position on a cell. However, over the entire cell, we observe large dispersion of pore sizes, owing to local differences in the transmembrane potential and the number of pores (Fig. 4, *A–C*). This comparison demonstrates that the spatial interactions have nontrivial effects on the process of cell electroporation, and that the behavior of a membrane patch differs in a substantial way from that of the entire cell.

DISCUSSION

The model presented here allows us to study both temporal and spatial aspects of cell electroporation without prohibitive computational costs. This section evaluates how well the results of the model match experiments.

In evaluation of the model, one needs to keep in mind that this study cannot even attempt to reproduce quantitatively the results of any particular experiment: it is not possible to find in the literature all parameters required by the model for a single cell type. Some parameters have been chosen to match the study of Hibino et al. (44), who used potentiometric dyes to visualize the evolution of transmembrane potential during electroporation of sea urchin eggs. That study provided us with values of the cell radius, intracellular and extracellular conductivity, membrane conductance, and threshold for electroporation. Other parameters listed in Table 1 came from other sources, many of them from experiments on artificial lipid bilayers. Thus, differences between the results of experiments and our model are to be expected.

Voltage

The most detailed information on the electroporation process in a cell came from measurements of V_m^θ using voltage-sensitive fluorescent dyes obtained by Hibino et al. (44). Observation of changes in fluorescence over the cell circumference as electroporation progresses provided us with the spatial distribution of V_m^θ and the timescale of its evolution. The model reproduces quite well the transmembrane potential V_m^θ measured in this study. Just like as seen in the experiment, in the model V_m^θ evolves on the timescale of microseconds, with the V_m^θ magnitude exhibiting the saturation characteristic of electroporation. The spatial distribution of V_m^θ is also similar: V_m^θ in the polar regions of the cell settles at a uniform value of $\sim\pm0.42$ V and has a larger magnitude near the border of the electroporated region. In both the model and the experiment, pore formation occurs first at the hyperpolarized pole owing to the negative rest potential.

In the experiment of Hibino et al. (44), the values of V_m^θ in the depolarized hemisphere, and also to a smaller degree in the hyperpolarized one, decrease in magnitude during the entire 1-ms pulse. In consequence, the cell potential exhibits a slow, depolarizing drift. No such drift is seen in the model: after the first 3 μs, V_m^θ at the two poles changes very little (Fig. 2 *A*). The possible origin of this drift and its consequences on the assessment of the membrane conductance are discussed below.

Number and spatial distribution of pores

It is usually assumed that most pores are created at the poles of the cell and that the number of pores decreases to zero near the equator. The model confirms this assumption (Fig. 3 *B*), and supplies a previously unknown observation that pores are much larger on the border of the electroporated region than at the poles (Fig. 3 *C*). This prediction is confirmed indirectly by the shape of the V_m^θ profile measured by Hibino et al. (44). In Fig. 4 of their article, V_m^θ not only flattens at the poles but with time also develops dips. This shape is reproduced by the model (Fig. 3 *A*), but only when the pores are allowed to grow. Our previous cell models, in which pore radii were kept constant, could reproduce only very small dips (24,46).

The model predicts that the pulse creates more but smaller pores on the hyperpolarized hemisphere and fewer but larger pores on the depolarized hemisphere. This prediction agrees with the experiment of Tekle et al. (5), in which small molecules (ethidium bromide and Ca^{2+}) entered predominantly through the hyperpolarized end, while larger ones (propidium iodide and ethidium homodimer) entered predominantly through the depolarized end.

Extent of electroporation

By imaging the uptake of propidium iodide, Gabriel et al. (6) have shown that the extent of the electroporated cell membrane increases with the pulse strength, and that the critical polar angle θ_c is slightly larger on the hyperpolarized hemisphere. The model agrees with this observation for field

strengths above 20 kV/m; for weaker fields, θ_h is actually smaller than θ_d (Fig. 8). This experiment also demonstrates that cos θ_c has a linear dependence on $1/E$. In the model, the fit to the straight line is better for θ_h than for θ_d (correlation coefficients are 0.989 and 0.962, respectively).

Some studies have used Eq. 12 for charging of a passive cell to evaluate which parts of the cell are electroporated (16–19). The underlying assumption is that wherever V_m^θ found from Eq. 12 exceeds threshold, the membrane will be electroporated. As seen in Fig. 8, which shows θ_d and θ_h together with their estimates from Eq. 12, this method overestimates the extent of electroporation by 20–32%, depending on the pulse strength. The reason for this discrepancy is that the creation of pores diminishes the magnitude of V_m^θ everywhere on the membrane, not only in the electroporated regions (Fig. 3 *A*). Thus, the cell never reaches V_m^θ predicted by Eq. 12, and consequently the extent of electroporation is smaller.

Distribution of pore radii

An interesting prediction of the model is the existence of two distinct pore populations, small and large, the former being more numerous and the latter contributing more to the total pore area. We are not aware of an experimental study that has confirmed this prediction. For example, the study of Chang and Reese, who used rapid-freezing electron microscopy to visualize the evolution of pores in red blood cells, could measure only pores with radii above 1 nm, so the small pore population was not seen (47). Nevertheless, this finding may aid in interpretation of experiments involving uptake of fluorescent molecules. Depending on their sizes, marker molecules may not permeate pores from both populations. In particular, DNA uptake was found to be most effective with weak pulses that exceed threshold only slightly (48–51). Since neither the number of large pores nor their area decreases substantially with pulse strength (Fig. 8, *B* and *D*), this finding can be related to the decrease in the average pore radius, $\bar{r}$ (Fig. 8 *C*). For pulses above 20 kV/m, $\bar{r}$ levels off just above 20 nm. Considering that the effective radius of DNA is 5–9 nm (52), 20 nm pores should allow DNA permeation but perhaps transport is not as efficient as with larger pores. Alternatively, transport may be sufficiently effective but long pulses required for the uptake (at least 1 ms (53,54)) increase the probability of cells dying. Possibly, this question can be resolved with real-time observations of DNA uptake (55).

The sizes of large pores measured by Chang and Reese (47) range from 20 to 120 nm, and this estimate is comparable with radii predicted by the model when a weak pulse of 15 kV/m is used (Fig. 8 *C*). However, there is an important difference: in the experiment, the pores were observed 40 ms *after* the pulse. The model predicts that by this time, all pores would have shrunk to the minimum-energy radius of ~0.8 nm (Fig. 5 *A*). While some researchers consider the pores observed by Chang and Reese (56) to be hemolysis pores induced by cell swelling, large electropores growing in the absence of the induced V_m have been observed in our model (13,30). This so-called postshock coarsening occurs when the initial tension of the membrane is high and when a weak pulse creates a subcritical number of pores.

Postpulse pore shrinkage

As seen in Fig. 5 *A*, within microseconds after the pulse termination, all pores shrink to the minimum-energy radius $r_m \approx 0.8$ nm, where they persist until resealing takes place. This shrinkage of pores explains the experimental observation that the permeable state is long-lived for small, but not large, molecules (54,57,58). It may also underlay the postpulse decrease in membrane conductance observed experimentally by Glaser et al. (39).

Fractional pore area and membrane conductance

The huge increase in membrane conductance G^θ caused by creation of pores makes it impossible for the cell to maintain its negative rest potential and hence the V_m^θ on the equator is very small. Thus, to assure that currents entering and leaving the cell balance, the conductances of both hemispheres should be equal, at least approximately. This indeed happens in the model: distributions of membrane conductances differ slightly (Fig. 6 *B*) but the total conductances are nearly equal: 0.468 and 0.455 mS for depolarized and hyperpolarized hemispheres, respectively. A study of Tekle et al. (59) concludes that the total area of pores at the two hemispheres could be quite similar even if there is asymmetry in pore number and their sizes. This conclusion clearly assumes that the area and conductance of pores are linearly related. In reality, the relationship between the pore area and conductance is strongly influenced by assumptions made in computing the current through a pore. Equation 5, which accounts for the decrease of the transpore voltage, predicts that pore conductance grows slower than linearly with the pore area. Thus, the model predicts different pore areas on the depolarized and hyperpolarized hemispheres (11.7 and 9.9 μm^2), even though their total conductances are approximately equal. The pore areas on the two hemispheres would be somewhat different if Eq. 5 incorporated interactions between ions and the pore walls.

It is much harder to reconcile the model's prediction with the results of Hibino et al. (44), who have inferred from their optical measurements of V_m^θ that the membrane conductance G^θ is asymmetric: G^D exceeds G^H by a factor of approximately two. This asymmetry can be traced to a slow drift of V_m^θ toward more positive values, which leads to depolarization of a cell. As stated above, this drift is not reproduced by the model. We have tested two hypotheses regarding its origin.

First, the cell may slowly depolarize because the current flowing through pores changes intracellular concentrations. To test this hypothesis, we have replaced Eq. 5 for a current through a pore by an ion-specific current composed of Na^+, K^+, Cl^-, and Ca^{2+} ions, and we have allowed intracellular concentrations of these ions to vary, using the methods described in our previous publication (46). The results demonstrate that the change of ionic concentrations affects the number and size of pores, but has very little effect on the distribution of either V_m^θ or G^θ. Most importantly, no slow depolarization of the cell is observed.

Second, the slow depolarization of a cell and the resulting asymmetry of G^θ may be an artifact of the experiment, such as dye bleaching or calibration of fluorescence signals. We have found out that the latter may offer a plausible explanation. Note from Fig. 7 that transmembrane potential on the cell equator has a small depolarized value, 0.021 V. An experimenter may easily ignore it and assume that V_m^E is zero. Consequently, voltages computed from fluorescence will be shifted by 0.021 V: the magnitude of V_m^θ will be decreased in the depolarized hemisphere and increased in the hyperpolarized hemisphere. If the shifted V_m^θ is used to compute membrane conductance, then G^D will be 6.1×10^4 S/m^2 and G^H will be 5.4×10^4 S/m^2, i.e., the same type of asymmetry as reported by Hibino et al. (7,44). However, Hibino et al. stress that they have *not* used the assumption that V_m^E is zero in processing their fluorescence data.

It is also possible that the slow depolarization of the cell may be due to factors not included in the model, such as exchange of charged molecules between the two monolayers of the membrane (60,61). However, conductivity estimates inferred from measurements made with voltage-sensitive dyes can now be independently verified. Recent development of microelectroporation devices has opened up a possibility of impedance measurements during electroporation of single cells (8). The model indicates that such measurements should be performed during the pulse to avoid large errors caused by the postpulse shrinking of pores. If impedance measurements are performed after the pulse with small, subthreshold pulses, then the measured G will reflect the membrane conductance seen in Fig. 5, which shows a postpulse G^θ that is considerably smaller than G^θ during the pulse.

Stages of electroporation

The stages of electroporation seen in the model closely resemble the steps of electropermeabilization identified by Teissié et al. based on experimental observations (56). The ''induction step'' corresponds to the charging and nucleation stages of the model, the ''expansion step'' corresponds to the pore evolution stage, the ''stabilization step'' corresponds to the postpulse shrinkage of pores, and the ''resealing step'' corresponds to the resealing of small pores described by Eq. 7 (not discussed in this article but demonstrated in our previous studies (13,24)). The only step not seen in the model is the ''memory effect'' that describes changes in the membrane and cell behavior persisting on the timescale of hours.

While some of the model's predictions still must be confirmed experimentally, the resemblance between the model's ''stages'' and ''steps'' of electroporation seen in experiments gives us a reason to believe that the single cell model presented here may be ready to provide theoretical support for real-life applications. For example, it can be used to design pulsing protocols. The model's ability to compute dynamically the size of pores and their distribution on the cell surface in response to a pulse of a given strength allows one to develop and test in silico protocols tailored to specific tasks: cell lysis, creation of large pores for DNA uptake or small pores for drug delivery, minimization of cell stress, etc. In addition, the model can relate the impedance signal measured in on-chip single cell electroporation devices to the underlying stages of the electroporation process. Thus, the model can provide a rational basis for extracting more information from the easily accessible impedance measurements.

This work was supported in part by the National Science Foundation grant No. BES-0401757.

REFERENCES

1. Potter, H. 1988. Electroporation in biology: methods, applications, and instrumentation. *Anal. Biochem.* 174:361–373.
2. Sukharev, S. I., V. A. Klenchin, S. M. Serov, L. V. Chernomordik, and Y. A. Chizmadzhev. 1992. Electroporation and electrophoretic DNA transfer into cells. The effect of DNA interaction with electropores. *Biophys. J.* 63:1320–1327.
3. Weaver, J. C., and Y. A. Chizmadzhev. 1996. Theory of electroporation: a review. *Bioelectrochem. Bioenerg.* 41:135–160.
4. Dev, S. B., D. P. Rabussay, G. Widera, and G. A. Hofmann. 2000. Medical applications of electroporation. *IEEE Trans. Plasma Sci.* 28: 206–223.
5. Tekle, E., R. D. Astumian, and P. B. Chock. 1994. Selective and asymmetric molecular transport across electroporated cell membranes. *Proc. Natl. Acad. Sci. USA.* 91:11512–11516.
6. Gabriel, B., and J. Teissié. 1997. Direct observation in the millisecond time range of fluorescent molecule asymmetrical interaction with the electropermeabilized cell membrane. *Biophys. J.* 73:2630–2637.
7. Hibino, M., M. Shigemori, H. Itoh, K. Nagayama, and K. Kinosita. 1991. Membrane conductance of an electroporated cell analyzed by submicrosecond imaging of transmembrane potential. *Biophys. J.* 59: 209–220.
8. Huang, Y., N. S. Sekhon, J. Borninski, N. Chen, and B. Rubinsky. 2003. Instantaneous, quantitative single-cell viability assessment by electrical evaluation of cell membrane integrity with microfabricated devices. *Sensors Actuat. A.* 105:31–39.
9. Pastushenko, V. F., Y. A. Chizmadzhev, and V. B. Arakelyan. 1979. Electric breakdown of bilayer lipid membranes: II. Calculations of the membrane lifetime in the steady-state diffusion approximation. *Bioelectrochem. Bioenerg.* 6:53–62.
10. Barnett, A., and J. C. Weaver. 1991. Electroporation: a unified, quantitative theory of reversible electrical breakdown and mechanical rupture in artificial planar bilayer membranes. *Bioelectrochem. Bioenerg.* 25:163–182.

11. Freeman, S. A., M. A. Wang, and J. C. Weaver. 1994. Theory of electroporation of planar bilayer membranes: predictions of the aqueous area, change in capacitance, and pore-pore separation. *Biophys. J.* 67:42–56.
12. Neu, J. C., and W. Krassowska. 1999. Asymptotic model of electroporation. *Phys. Rev. E.* 59:3471–3482.
13. Smith, K. C., J. C. Neu, and W. Krassowska. 2004. Model of creation and evolution of stable macropores for DNA delivery. *Biophys. J.* 86: 2813–2826.
14. Weaver, J. C. 1994. Theory of electroporation. *Adv. Chem. Ser.* 235: 447–470.
15. Joshi, R. P., and K. H. Schoenbach. 2000. Electroporation dynamics in biological cells subjected to ultrafast electrical pulses: a numerical simulation study. *Phys. Rev. E.* 62:1025–1033.
16. Serša, G., M. Čemažar, D. Šemrov, and D. Miklavčič. 1996. Changing electrode orientation improves the efficacy of electrochemotherapy of solid tumor in mice. *Bioelectrochem. Bioenerg.* 39:61–66.
17. Saulis, G. 1993. Cell electroporation. Part 3. Theoretical investigation of the appearance of asymmetric distribution of pores on the cell and their further evolution. *Bioelectrochem. Bioenerg.* 32:249–265.
18. Neumann, E., S. Kakorin, I. Tsoneva, B. Nikolova, and T. Tomov. 1996. Calcium-mediated DNA adsorption to yeast cells and kinetics of cell transformation by electroporation. *Biophys. J.* 71:868–877.
19. Kotnik, T., and D. Miklavčič. 2006. Theoretical evaluation of voltage inducement on internal membranes of biological cells exposed to electric fields. *Biophys. J.* 90:480–491.
20. Pavlin, M., and D. Miklavčič. 2003. Effective conductivity of a suspension of permeabilized cells: a theoretical analysis. *Biophys. J.* 85: 719–729.
21. Davalos, R. V., B. Rubinsky, and D. M. Otten. 2002. A feasibility study for electrical impedance tomography as a means to monitor tissue electroporation for molecular medicine. *IEEE Trans. Biomed. Eng.* 49:400–403.
22. Puc, M., T. Kotnik, L. M. Mir, and D. Miklavčič. 2003. Quantitative model of small molecules uptake after in vitro cell electropermeabilization. *Bioelectrochemistry.* 60:1–10.
23. Gowrishankar, T. R., and J. C. Weaver. 2003. An approach to electrical modeling of single and multiple cells. *Proc. Natl. Acad. Sci. USA.* 100:3203–3208.
24. DeBruin, K. A., and W. Krassowska. 1999. Modeling electroporation in a single cell. I: Effects of field strength and rest potential. *Biophys. J.* 77:1213–1224.
25. Stewart, D. A., T. R. Gowrishankar, and J. C. Weaver. 2004. Transport lattice approach to describing cell electroporation: use of a local asymptotic model. *IEEE Trans. Plasma Sci.* 32:1696–1708.
26. Gowrishankar, T. R., A. T. Esser, Z. Vasilkoski, K. C. Smith, and J. C. Weaver. 2006. Microdosimetry for conventional and supra-electroporation in cells with organelles. *Biochem. Biophys. Res. Commun.* 341:1266–1276.
27. Joshi, R. P., Q. Hu, K. H. Schoenbach, and S. J. Bebe. 2002. Simulations of electroporation dynamics and shape deformations in biological cells subjected to high voltage pulses. *IEEE Trans. Plasma Sci.* 30:1536–1546.
28. Joshi, R. P., Q. Hu, and K. H. Schoenbach. 2004. Modeling studies of cell response to ultrashort, high-intensity electric fields—implications for intracellular manipulation. *IEEE Trans. Plasma Sci.* 32:1677–1686.
29. Hu, Q., S. Viswanadham, R. P. Joshi, K. H. Schoenbach, S. J. Beebe, and P. F. Blackmore. 2005. Simulations of transient membrane behavior in cells subjected to a high-intensity ultrashort electric pulse. *Phys. Rev. E.* 71:031914.
30. Neu, J. C., and W. Krassowska. 2003. Modeling postshock evolution of large electropores. *Phys. Rev. E.* 67:1–12.
31. Neu, J. C., K. C. Smith, and W. Krassowska. 2003. Electrical energy required to form large conducting pores. *Bioelectrochem. Bioenerg.* 60:107–114.
32. Chernomordik, L. V., S. I. Sukharev, I. G. Abidor, and Y. A. Chizmadzhev. 1983. Breakdown of lipid bilayer membranes in an electric field. *Biochim. Biophys. Acta.* 736:203–213.
33. Sakuma, I., T. Haraguchi, K. Ohuchi, Y. Fukui, I. Kodama, J. Toyama, N. Shibata, and S. Hosoda. 1998. A model analysis of aftereffects of high-intensity DC stimulation on action potential of ventricular muscle. *IEEE Trans. Biomed. Eng.* 45:258–267.
34. DeBruin, K. A., and W. Krassowska. 1998. Electroporation and shock-induced transmembrane potential in a cardiac fiber during defibrillation strength shocks. *Ann. Biomed. Eng.* 26:584–596.
35. Ashihara, T., and N. A. Trayanova. 2004. Asymmetry in membrane responses to electric shocks: insights from bidomain simulations. *Biophys. J.* 87:2271–2282.
36. Sambelashvili, A. T., V. P. Nikolski, and I. R. Efimov. 2004. Virtual electrode theory explains pacing threshold increase caused by cardiac tissue damage. *Am. J. Physiol.* 286:H2183–H2194.
37. Newman, J. 1966. Resistance for flow of current to a disk. *J. Electrochem. Soc.* 113:501–502.
38. Powell, K. T., E. G. Derrick, and J. C. Weaver. 1986. A quantitative theory of reversible electrical breakdown of bilayer membranes. *Bioelectrochem. Bioenerg.* 15:243–255.
39. Glaser, R. W., S. L. Leikin, L. V. Chernomordik, V. F. Pastushenko, and A. I. Sokirko. 1988. Reversible electrical breakdown of lipid bilayers: formation and evolution of pores. *Biochim. Biophys. Acta.* 940:275–287.
40. Barnett, A. 1990. The current-voltage relation of an aqueous pore in a lipid bilayer membrane. *Biochim. Biophys. Acta.* 1025:10–14.
41. Melikov, K. C., V. A. Frolov, A. Ahcherbakov, A. V. Samsonov, and Y. A. Chizmadzhev. 2001. Voltage-induced nonconductive and metastable pores in unmodified lipid bilayers. *Biophys. J.* 80:1829–1836.
42. Benz, R., and U. Zimmermann. 1980. Relaxation studies on cell membranes and lipid bilayers in the high electric field range. *Bioelectrochem. Bioenerg.* 7:723–739.
43. Powell, K. T., A. W. Morgenthaler, and J. C. Weaver. 1989. Tissue electroporation. Observation of reversible electrical breakdown in viable frog skin. *Biophys. J.* 56:1163–1171.
44. Hibino, M., H. Itoh, and K. Kinosita. 1993. Time courses of cell electroporation as revealed by submicroscopic imaging of transmembrane potential. *Biophys. J.* 64:1789–1800.
45. Bier, M., S. M. Hammer, D. J. Canaday, and R. C. Lee. 1999. Kinetics of sealing for transient electropores in isolated mammalian skeletal muscle cells. *Bioelectromagnetics.* 20:194–201.
46. DeBruin, K. A., and W. Krassowska. 1999. Modeling electroporation in a single cell. II: Effects of ionic concentrations. *Biophys. J.* 77:1225–1233.
47. Chang, D. C., and T. S. Reese. 1990. Changes in membrane structure induced by electroporation as revealed by rapid-freezing electron microscopy. *Biophys. J.* 58:1–12.
48. Hama-Inaba, H., M. Takahashi, M. Kasai, T. Shiomi, A. Ito, F. Hanaoka, and K. Sato. 1987. Optimum conditions for electric pulse mediated gene transfer to mammalian cells in suspension. *Cell Struct. Funct.* 12:173–180.
49. Rols, M.-P., C. Delteil, M. Golzio, P. Dumond, S. Cros, and J. Teissié. 1998. In vivo electrically mediated protein and gene transfer in murine melanoma. *Nat. Biotechnol.* 16:168–171.
50. Gehl, J., and L. M. Mir. 1999. Determination of optimal parameters for in vivo gene transfer by electroporation, using a rapid in vivo test for cell permeabilization. *Biochem. Biophys. Res. Commun.* 261:377–380.
51. Yoshizato, K., T. Nishi, T. Goto, S. B. Dev, H. Takeshima, T. Kino, K. Tada, T. Kimura, S. Shiraishi, M. Kochi, J.-I. Kuratsu, G. A. Hofmann, and Y. Ushio. 2000. Gene delivery with optimized electroporation parameters shows potential for treatment of gliomas. *Int. J. Oncol.* 16:899–905.
52. Rybenkov, V. V., A. V. Vologodskii, and N. R. Cozzarelli. 1997. The effect of ionic conditions on the conformations of supercoiled DNA: I. Sedimentation analysis. *J. Mol. Biol.* 267:299–311.
53. Klenchin, V. A., S. I. Sukharev, S. M. Serov, L. V. Chernomordik, and Y. A. Chizmadzhev. 1991. Electrically induced DNA uptake by cells is a fast process involving DNA electrophoresis. *Biophys. J.* 60:804–811.

54. Rols, M.-P., and J. Teissié. 1998. Electropermeabilization of mammalian cells to macromolecules: control by pulse duration. *Biophys. J.* 74:1415–1423.

55. Phez, E., C. Faurie, M. Golzio, J. Teissié, and M.-P. Rols. 2005. New insights in the visualization of membrane permeabilization and DNA/membrane interaction of cells submitted to electric pulses. *Biochim. Biophys. Acta.* 1724:248–254.

56. Teissié, J., M. Golzio, and M.-P. Rols. 2005. Mechanisms of cell membrane electropermeabilization: a minireview of our present (lack of?) knowledge. *Biochim. Biophys. Acta.* 1724:270–280.

57. Wolf, H., M.-P. Rols, E. Boldt, E. Neumann, and J. Teissié. 1994. Control by pulse parameters of electric field-mediated gene transfer in mammalian cells. *Biophys. J.* 66:524–531.

58. Satkauskas, S., M. F. Bureau, M. Puc, A. Mahfoudi, D. Scherman, D. Miklavčič, and L. M. Mir. 2002. Mechanisms of *in vivo* DNA electrotransfer: respective contributions of cell electropermeabilization and DNA electrophoresis. *Mol. Ther.* 5:133–140.

59. Tekle, E., R. D. Astumian, W. A. Friauf, and P. B. Chock. 2001. Asymmetric pore distribution and loss of membrane lipid in electroporated DOPC vesicles. *Biophys. J.* 81:960–968.

60. Haest, C. W. M., D. Kamp, and B. Deuticke. 1997. Transbilayer reorientation of phospholipid probes in the human erythrocyte membrane. Lessons from studies on electroporated and resealed cells. *Biochim. Biophys. Acta.* 1325:17–33.

61. Vernier, P. T., Y. Sun, L. Marcu, C. M. Craft, and M. A. Gundersen. 2004. Nanopulse-induced phosphatidylserine translocation. *Biophys. J.* 86:4040–4048.

62. Chambers, E. L., and J. de Armendi. 1979. Membrane potential, action potential and activation potential of eggs of the sea urchin, *Lytechinus variegatus. Exp. Cell Res.* 122:203–218.

63. Hénon, S., G. Lenormand, A. Richert, and F. Gallet. 1999. A new determination of the shear modulus of the human erythrocyte membrane using optical tweezers. *Biophys. J.* 76:1145–1151.

64. Israelachvili, J. 1992. Intermolecular and Surface Forces, 2nd Ed. Academic Press, London, UK.